Preparation of a Poly(methyl methacrylate)/Ultrahigh Molecular Weight Polyethylene Blend Using Supercritical Carbon Dioxide and the Identification of a Three-Phase Structure: An Atomic Force Microscopy Study

Jianxin Zhang,*,† Andrew J. Busby,‡ Clive J. Roberts,† Xinyong Chen,† Martyn C. Davies,† Saul J. B. Tendler,† and Steven M. Howdle‡

Laboratory of Biophysics and Surface Analysis, School of Pharmaceutical Sciences, and School of Chemistry, University of Nottingham, Nottingham, NG7 2RD, UK

Received December 28, 2001

ABSTRACT: Supercritical carbon dioxide ($scCO_2$) has been used as the processing medium to facilitate effective impregnation and subsequent polymerization of methyl methacrylate monomer in ultrahigh molecular weight polyethylene (UHMWPE), providing a route to new nanocomposite materials. In this paper, the morphological structures of UHMWPE, $scCO_2$-treated UHMWPE, and a blend of (53/47 w/w) UHMWPE/poly(methyl methacrylate) (PMMA) prepared in $scCO_2$ are investigated using tapping mode atomic force microscopy (TMAFM). Under moderate tapping conditions, phase imaging offers a good contrast of the nanostructures of the semicrystalline polymers due to a large difference in stiffness between the crystalline and amorphous phases. This is demonstrated by a TMAFM force mode characterization method through amplitude−phase−distance (APD) measurements on the nanoscale crystalline and amorphous domains. The use of this method has also identified that the UHMWPE/PMMA blend consists of three phases: UHMWPE crystalline, UHMWPE amorphous, and PMMA amorphous. These three phases display three different characteristic tip−sample interaction profiles. The phase-segregated PMMA domains are estimated to be between 10 and 100 nm in size. In addition, it is found that the blending method via in-situ polymerization has significantly increased the crystallinity of the UHMWPE. The increase in crystallinity, together with the appearance of a second low melting temperature endothermic peak in differential scanning calorimetry (DSC) analysis of the UHMWPE/PMMA blend, is consistent with the increased population of small crystallites observed in the AFM phase images. We attribute this effect to the enhanced mobility of UHMWPE molecules caused by $scCO_2$ impregnation and addition of the PMMA component. Through statistical analysis of the phase distribution in the APD data our results also demonstrate that the crystallinity of polymers can be quantified by using phase imaging analysis at 48.3% for UHMWPE, 52.2% for treated $scCO_2$, and 32.8% for UHMWPE/PMMA (i.e., 61.9% of the UHMWPE component). These data are within 5% agreement with standard DSC bulk analysis of crystallinity.

I. Introduction

This paper describes the use of supercritical carbon dioxide ($scCO_2$) in the production of a blend of ultrahigh molecular weight polyethylene (UHMWPE) and poly(methyl methacrylate) (PMMA) at a temperature significantly below the usual processing temperature of UHMWPE. We describe a modification of the supercritical methodology first employed by Watkins and McCarthy,[1] combined with tapping mode atomic force microscopy (TMAFM) analysis to produce and characterize the first controlled blend of a methacrylate polymer with UHMWPE. The composite was found to exhibit phase-separated domains of PMMA with estimated sizes of 10−100 nm—much smaller than those observed for blends of UHMWPE reported elsewhere in the literature.[2,3] In addition, the two-step procedure described by Watkins and McCarthy[1] was modified so that only one step was required, with autoclave design and reaction conditions carefully controlled to provide "clean" blends requiring no further processing.

UHMWPE was chosen for this study because it exhibits a number of desirable mechanical and chemical characteristics, including high tensile and impact strength, good chemical resistance, and excellent wear properties.[4] However, its modification by incorporation of a second polymer has been limited by difficulties associated with its processing—its high molecular weight and resulting high viscosity mean that melt processing the polymer is not practical, and lack of solubility in common organic solvents means even solution casting is difficult. Despite these difficulties, a limited number of blends of other polymers with UHMWPE have been reported in the literature.[2,3] However, all of these blends display phase separation on the micron scale. Moreover, preparation requires high temperatures (up to 250 °C[3]) and the use of either organic solvents at high temperature or extreme shear forces during melt processing to achieve acceptable mixing of the phases. In this paper we show that $scCO_2$ provides an excellent medium for processing this polymer at temperatures significantly below those of conventional melt processing methods.

Supercritical CO_2 has recently attracted great interest as a medium for polymer processing and synthesis[1,5−11] due to its unique combination of gaslike and liquidlike properties. Like gases, it has high diffusivity and low viscosity, like liquids it can dissolve a range of compounds and small molecules. Supercritical carbon dioxide is a good swelling agent[5,7] and generally a poor

* Corresponding author: Tel +44 (0) 115 9515048; Fax +44 (0) 115 9515110; e-mail Jianxin.Zhang@nottingham.ac.uk.
† School of Pharmaceutical Sciences.
‡ School of Chemistry.

10.1021/ma012258v CCC: $22.00
Published on Web 10/05/2002

solvent for most polymers.[6] These properties make it an ideal medium for yielding polymer composites. This may be achieved by supercritical impregnation of a monomer into a host polymer followed by in-situ polymerization within the polymer matrix.[1,9,10] Fast removal of the solvent from the final product upon depressurization is equivalent to quenching, making it possible to produce a blend of a thermodynamically immiscible polymer pair with a fine morphology. Unlike conventional processing methods, the use of CO_2 leaves no toxic solvent residues,[5,6] making it particularly suitable for preparation of polymeric materials for biomedical applications.

Several groups have studied the interaction of high pressure and supercritical CO_2 with polymers. Shieh et al.[11] observed that CO_2 often results in an increase in the crystallinity and a decrease in the glass transition temperature (T_g) of polymers exposed to it, which translates into the change in the yield strength and elastic modulus. McCarthy and colleagues[1,9,10] have carried out extensive studies in a range of polymer systems. Recently, they detailed a morphological and mechanical investigation of polystyrene (PS)/high-density polyethylene (HDPE) composites.[10] They observed that PS resided throughout the interlamellar regions of the HDPE spherulites and preferentially aggregated in the spherulite center. However, the crystalline region was not affected. The mechanical strength and modulus of the resulting composites were dramatically improved at the expense of their toughness.

Understanding the morphological structures of polymers and polymer blends is crucial in the development of a new generation of polymer composites since such structures influence the properties of the resulting materials. Atomic force microscopy (AFM) can be employed to provide direct spatial mapping of a material's surface morphology at the nanometer scale. In particular, TMAFM is ideal for this approach and is capable of imaging soft samples like biological and polymeric materials with minimal distortion.[12−18] TMAFM involves a brief and intermittent tip−sample contact in each cantilever oscillation cycle during scanning. The phase lag of the cantilever oscillation compared to the driving signal has been shown to be sensitive to the local materials properties such as stiffness,[12,13] viscoelasticity,[14,15] and chemical heterogeneity.[15,17] However, there are a number of other factors[12,19,20] that could affect the phase image. Because of these complex variables, care must be taken in the collection of these images. It is generally believed that the TMAFM phase image contrast is associated with the energy dissipated by the tip−sample interactions;[21] however, the relationship between the energy dissipation and materials properties is difficult to quantify.

TMAFM can also operate in a localized nonimaging force mode[15] or dynamic force spectroscopy mode,[22] whereby the tip−sample interactions as a function of the relative tip−sample distance are measured. Briefly, during an experiment, the probe is vertically moved over a selected point of a sample surface, instead of laterally scanning an area. The quantities it records are normally the amplitude and phase against scanner motion. This type of measurement can be used to study the molecular attraction and repulsion between the sample and tip and has been shown to be very useful in explaining height artifacts and reversal of phase contrast[12,19] and in identifying different components in heterogeneous samples.[17,18,23]

In this paper we characterize the morphological structures of a biomedical-grade UHMWPE consolidate and its blend with PMMA by using TMAFM. The blend was prepared by $scCO_2$-assisted impregnation of methyl methacrylate (MMA) monomer into UHMWPE followed by in-situ polymerization. To help interpret the results from TMAFM analysis, differential scanning calorimetry (DSC) analysis was also carried out on the samples.

II. Experimental Section

Materials. The UHMWPE used in this study was GUR 1050 in round bar stocks with a diameter of 25 mm machined down to give disks 15 mm in diameter and 2 mm thick. The bars were ram extruded by Perplas Medical Ltd. (Bacup, UK). These samples had been air-annealed by the supplier (specific conditions unknown). The density of the sample material was 930 g cm^{-3} with $M_w \sim 7 \times 10^6$ g mol^{-1}. The samples were medical grade fabricated with no additional stabilizers or processing aids. MMA [ICI; inhibited with 2 ppm Topanol (a mixture of hindered amines)] and the initiator, *tert*-butyl peroxybenzoate (Aldrich), were used as received. CO_2 (BOC gases, SFC grade) was used as the solvent for the reaction. N_2 (BOC gases, oxygen free) was used for leak testing and to purge oxygen from the system prior to reaction.

Synthesis Procedure. Polymerization was performed in 60 mL stainless steel autoclave (NWA GmbH), which was modified extensively at the University of Nottingham. In a typical experiment the autoclave was charged with MMA (5 g) and *tert*-butyl peroxybenzoate (0.05 g, 1 wt % with respect to monomer); two disks of UHMWPE (∼0.34 g each) were suspended within in it and sealed. The apparatus was then pressurized with N_2 to 3000 psi—this was both to leak test the apparatus and to degas the reactants. Following careful release of the N_2, the reactor was filled with liquid CO_2 and heated to the desired temperature using a thermocouple-controlled aluminum heating block. The desired working pressure was obtained by adding more CO_2 into the system as required.

Reactions were performed at 120 °C and 3000 psi, with the reactor typically taking a period of 45 min to achieve the desired temperature. The samples used in this study were processed for 16 h to ensure that the polymerization reaction was complete; however, significant loadings of PMMA were obtained after as little as 2 h processing time. The reaction was stirred throughout by a magnetically coupled stirrer operating at 50 rpm. This was found to be necessary; otherwise, a large amount of polymer was deposited on the outside of the disks, which then required a subsequent washing step to remove. The composition of the blend was determined gravimetrically after removing the blend from the reactor and ensuring that any loose PMMA was removed from the surface of the UHMWPE disk by wiping with a dry cloth. A degree of swelling of the UHMWPE disk was observed, but no foaming or distortion. The procedure for running the control sample was identical, except neither monomer nor initiator was added to the autoclave prior to pressurization. After the completion of the synthesis or $scCO_2$ treatment of the UHMWPE sample, the autoclave was allowed to cool to room temperature over a period of 60 min. The CO_2 was then vented over a period of 30 s. Pure PMMA simultaneously synthesized in the fluid phase was obtained from the bottom of the autoclave. The pure PMMA was used as a signature control for AFM to "fingerprint" its existence in the blend.

AFM Characterization. Figure 1 shows schematically the method used to obtain specimens for AFM examination. Thin sections of about 1 mm thickness were cut from the sample disk with a razor. The surface of each sectioned specimen that was parallel to the $x-z$ plane (see Figure 1) was cryomicrotomed (RMC MT-7 cryoultramicrotome) along the extrusion direction at −130 °C using a glass knife. The flat and smooth surfaces were generated with an initial rough trimming

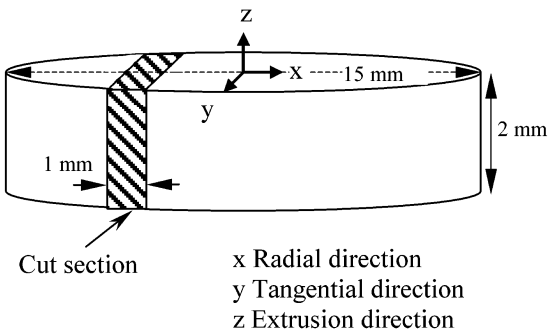

Figure 1. Schematic of a sample disk and sampling location, showing that the surfaces of the samples microtomed and subsequently examined are parallel with the UHMWPE axial or extrusion direction.

followed by cutting off thin sections down to 50 nm. To generate a flat surface of pure PMMA, a small amount of PMMA was sandwiched between two cleaned glass slides, softened at ~130 °C for about 3 min on a hot plate, and allowed to cool while a slight load was applied on the top glass. PMMA thin film (ca. 0.5 mm thick) with smooth surface was then obtained by removing the glass slides.

TMAFM experiments were performed using Nanoscope IIIa controlled Dimension 3000 AFM (Digital Instrument, Santa Barbara, CA). Commercial silicon cantilever probes, with a nominal tip radius of less than 10 nm (Nanoscope Olympus, 160 μm cantilever length and spring constant ranging 12−103 N m^{-1}), were employed just under their fundamental resonance frequencies of about 300 kHz. Height and phase images were acquired simultaneously under ambient conditions. To remove possible contamination on the AFM tips and improve the reproducibility of the results, the probes were treated in an argon plasma gas (RF Plasma Barrel Etcher) prior to each experiment. Scan rates were set at 2 Hz on all images. The free cantilever vibration amplitude (A_0) was fixed at 31 nm. Imaging data from TMAFM very much depends on the level of tapping force that is applied onto a sample surface by the probe apex. The tapping strength under a certain A_0 can be expressed as a ratio (r_{sp}) of the set point amplitude (A_{sp}) to A_0, with higher r_{sp} indicating lighter tapping and lower r_{sp} heavier tapping. Light tapping is normally used to acquire height images to reduce the possibility of height artifacts.[12,19] In this study a moderate tapping strength of 0.79 was chosen to obtain phase images.

After the phase images were obtained, amplitude−phase−distance (APD) curves were measured on different characteristic positions of all the samples. The detector sensitivity was calibrated using the contact part of the amplitude−distance curves measured on a mica surface. Apart from sample surface properties, the APD data can be also strongly affected by tip characteristics such as tip-end geometry, tip chemistry, and spring constant,[20] which are difficult to quantify. To make the data comparable, all the images and APD curves presented in this paper were acquired using the same tip. The raw phase data recorded in Nanoscope IIIa were decoded and transformed to a value of degrees according to $\varphi_d = \cos^{-1}(\varphi_r/32768)180/\pi$, where φ_d is the phase angle in degrees and φ_r is the phase angle recorded as a 16-bit signed integer. All the phase images remain unprocessed whereas the height images were processed to improve their clarity.

DSC Characterization. A Perkin-Elmer DSC7 calorimeter was employed to determine the melting temperatures, the heat of fusion, and the glass transition temperature of the samples. The DSC heating scans were carried out at a heating rate of 10 °C min^{-1} under a nitrogen gas flow on samples weighing approximately 5 mg. The DSC was calibrated using indium prior to the experiment. The crystallinity, X_c, of the samples were calculated using the following formula:

$$X_c = \frac{\Delta H_f}{\Delta H_{100}} \times 100 \quad (1)$$

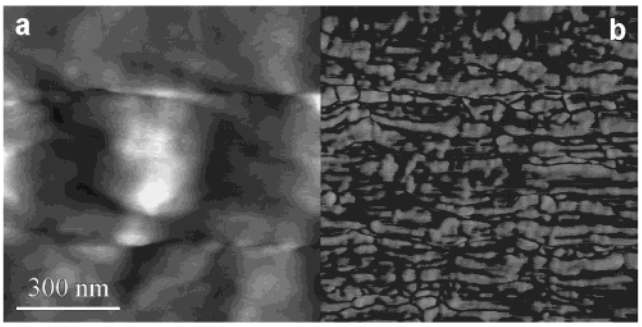

Figure 2. 1 μm × 1 μm TMAFM height (a) and phase (b) images of as-received UHMWPE. The images were taken on a cryomicrotomed surface with a free amplitude A_0 = 31 nm and set point r_{sp} = 0.79. The full gray scales cover 80 nm (a) and 90° (b) (in DI convention). The bright regions are identified as crystalline phase and the dark regions as amorphous phase.

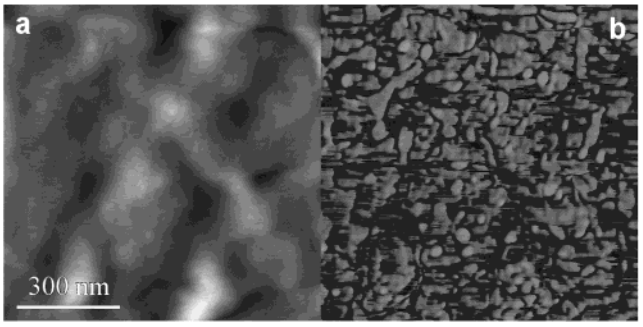

Figure 3. 1 μm × 1 μm TMAFM height (a) and phase (b) images of $scCO_2$-treated UHMWPE. The images were taken on a cryomicrotomed surface with a free amplitude A_0 = 31 nm and set point r_{sp} = 0.79. The full gray scales cover 80 nm (a) and 90° (b) (in DI convention).

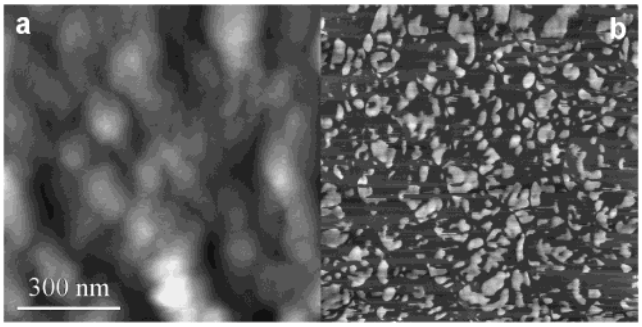

Figure 4. 1 μm × 1 μm TMAFM height (a) and phase (b) images of (53/47 w/w) UHMWPE/PMMA blend. The images were taken on a cryomicrotomed surface with a free amplitude A_0 = 31 nm and set point ratio r_{sp} = 0.79. The full gray scales cover 80 nm (a) and 90° (b) (in DI convention).

where ΔH_f is the heat of fusion of the semicrystalline sample and ΔH_{100} is the heat of fusion for 100% crystalline polyethylene, taken as 293 J g^{-1}.[24]

III. Results and Discussion

Figures 2−4 presents the height and phase images of as-received UHMWPE, $scCO_2$-treated UHMWPE, and 53/47 (w/w) UHMWPE/PMMA blend, respectively. These 1 × 1 μm images were acquired from the microtomed surfaces of these polymer samples under identical conditions using the same tip (see Experimental Section). It is noted from the height images in Figures 2a and 3a that the microtomed surface of the as-received UHMWPE is rougher than that of the $scCO_2$-treated sample. This may indicate that the $scCO_2$ impregnation

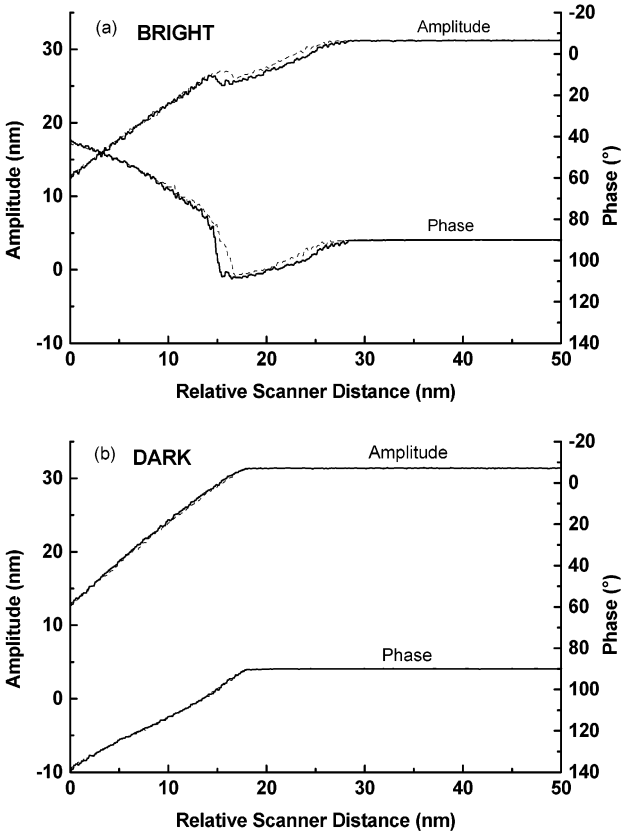

Figure 5. APD curves of as-received UHMWPE to identify crystalline phase (a) and amorphous phase (b). The significant difference in tip−sample interactions between these two phases is clearly shown. The solid lines are approach data, and the dashed lines are retract data.

assists in producing a more homogeneous internal structure of the polymer. Figure 4a shows a granular-shaped feature of the UHMWPE/PMMA blend, which is different from those of the other two samples. This change in the topography is probably due to the incorporation and precipitation of PMMA into UHMWPE, which results in the change in the UHMWPE internal structure. Apart from this, little information about the morphologies of the samples examined can be deduced from these height images. The corresponding phase images in Figures 2−4 show a strong contrast of bright and dark regions in all three samples. This is consistent with the fact that UHMWPE and the blend are semicrystalline polymers consisting of crystalline and amorphous phases with different moduli. However, it is not possible without detailed analysis to positively assign these two regions to specific phases or domains. This is because the assignment of bright and dark contrast to different phases is not always straightforward. Some studies[25] have revealed that the bright regions may be attributed to the stiffer material and the dark region to the softer, while a reversal has been reported from others.[12,26] In view of this, amplitude−phase−distance data were measured on locations within these two distinct regions since this measurement can provide additional information on localized properties of a sample.

Figure 5 shows typical APD curves for the "bright" (a) and "dark" (b) regions of the pure as-received UHMWPE. These two curves display significant differences in tip−sample interactions between these two regions. In the beginning of the APD curve measurements, the amplitude and phase data have values of 31 nm and 90°, respectively, when the tip has no interactions with the sample surface. These values remained constant until the tip made light contact with the sample, where attractive forces between the tip and sample exceed repulsive forces. As a consequence, the amplitude decreases, accompanied by an increase in phase lag to greater than 90°. This trend continued as the tip approached the sample further, until a certain point where a small increase in amplitude was observed before it continued to decrease linearly. Accordingly, a sudden change from greater than to less than 90° was observed in the phase shift, followed by a continuous decrease indicating that repulsive forces begin to dominate the tip−sample interactions at this transition point.[19] This process is evident for the bright region in Figure 5a. In the case of the dark region (Figure 5b), no such transition point was observed for the whole range of the probe vertical movement. Both amplitude and phase monotonically decreased when the tip gradually approached the sample, indicating that the attractive forces dominated the tip−sample interactions throughout. Note that the measuring ranges on both surface regions were the same; i.e., the vertical probe movement was stopped when the amplitude was reduced from its free level 31 nm to 13 nm.

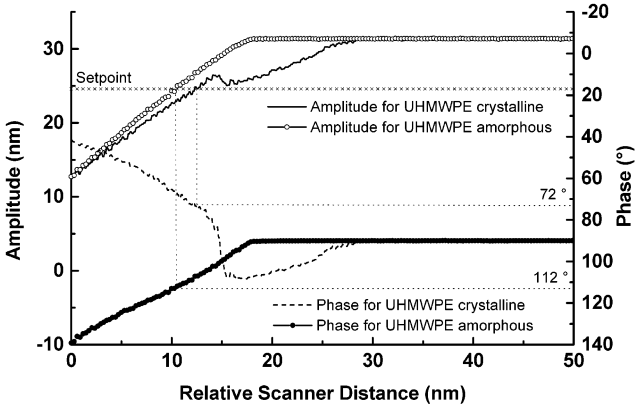

Figure 6. APD curves of the approach data from the two domains of as-received UHMWPE in Figure 2b. These curves demonstrate that the strong phase contrast achieved in Figure 2b is produced by the dramatic difference of the tip−sample interactions between the two domains at the set point amplitude A_{sp} = 24.5 nm.

We propose that this difference in the APD curve profile results from the variation in the mechanical properties of the different regions of the sample because these two regions are chemically identical. Therefore, it is not unreasonable to assign the bright region (Figure 2b) to the crystalline phase as it possesses a relatively high modulus and hence will exhibit a strong repulsive force on deformation to the tip and the dark region to the amorphous phase since it is in a rubbery state and such repulsive forces will be absent. Figure 6 shows that the difference between the crystalline phase (ca. 72°) and the amorphous phase (ca. 112°) is about 40° at the set point amplitude 24.5 nm. This explains the phase contrast of UHMWPE observed in Figure 2b in a numerical value. A similar conclusion can be made for the $scCO_2$-treated UHMWPE (Figure 3b).

After the successful identification of the two mechanically heterogeneous domains of UHMWPE, APD measurements were also carried out on the bright and dark regions of the UHMWPE/PMMA phase image (Figure

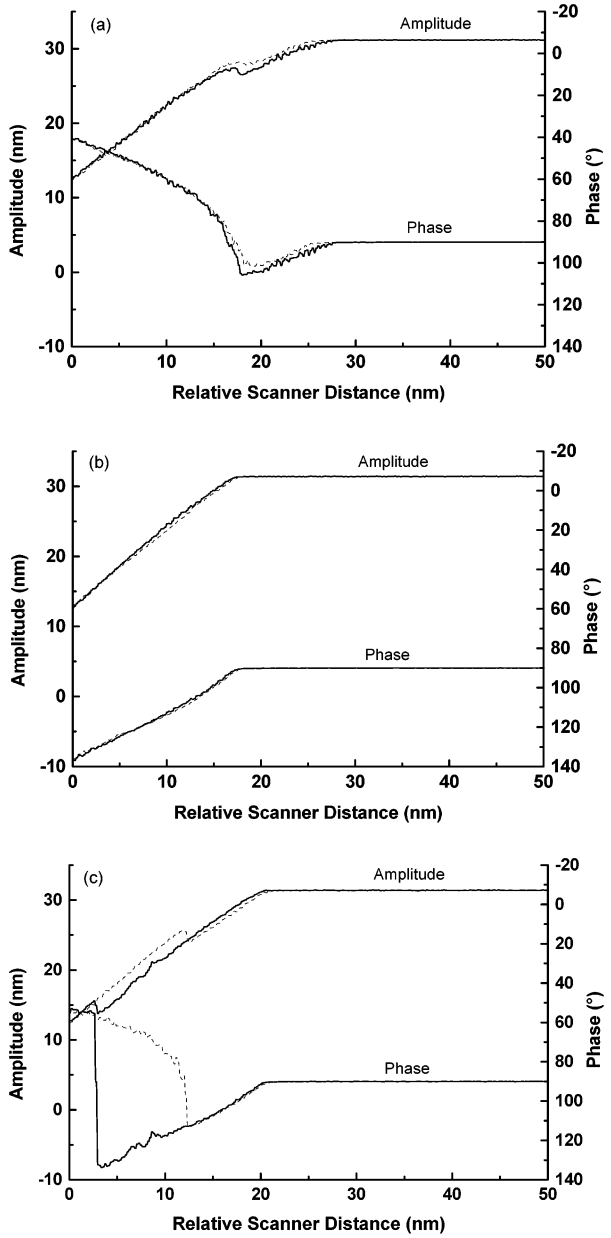

Figure 7. Three characteristic APD curves obtained from (53/47 w/w) UHMWPE/PMMA blend. Curves a, b, and c are identified to be the UHMWPE crystalline, UHMWPE amorphous, and amorphous PMMA phases, respectively. Note that Figure 7a,b matches Figure 5a,b, whereas Figure 7c matches Figure 8c. The solid lines are approach data, and the dashed lines are retract data.

4b). The results are presented in Figure 7. It was found that there are three types of curves with different profiles obtained from the blend. Note that the occurrence of these curves has been repeatedly tested on many different areas of the sample with different tips. Slight variations in the shapes of these curves acquired under the similar free amplitude level were observed, but the characteristics of the three different curves did not change. One of the underlying reasons for using the identical tip in the current study is to make the data presented here easily understood.

We propose that these three curves originate from three different domains in the blend. To confirm this assumption, comparisons are made between pure components and UHMWPE/PMMA. It is shown that the profiles of the APD curves (Figure 7a) measured in the

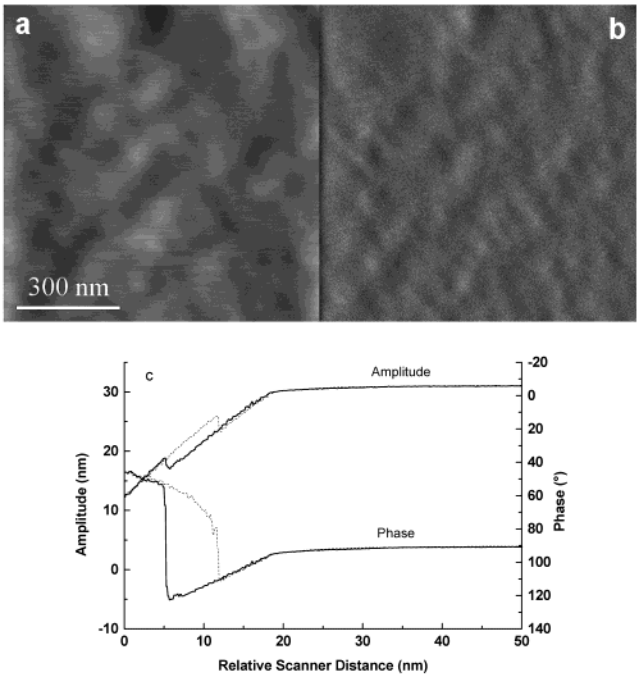

Figure 8. 1 μm $\times$ 1 μm TMAFM height image (a), phase image (b), and APD curves (c) of pure PMMA. The PMMA was simultaneously produced in the autoclave during in-situ synthesis of PMMA in UHMWPE. The full gray scales cover 10 nm (a) and 6° (b). (c) indicates no phase contrast for the homogeneous PMMA. The solid lines are approach data, and the dashed lines are retract data.

bright area of the blend phase image (Figure 4b) match well to those (Figure 5a) from the bright region of the pure UHMWPE, thus indicative of the crystalline phase of UHMWPE. It is possible to assign the other two curves (Figure 7b,c) that are observed in the dark region of the phase image using the same method. Thus, it is reasonable to propose that data such as in Figure 7b arise from UHMWPE amorphous domains since Figure 7b is clearly comparable to Figure 5b. Hence, it is conjectured that the trace in Figure 7c can be attributed to the PMMA component in the blend. To test this, the phase image and the APD curves of a pure PMMA film were acquired as shown in Figure 8. The phase image (Figure 8b) displays no contrast, as the PMMA is a homogeneous polymer. It is found by comparison that the APD curves as shown in Figures 8c and 7c are very similar to each other. Therefore, we propose that the blend consists of three phases: UHMWPE crystalline in the bright areas of the phase image and the UHMWPE amorphous and PMMA amorphous that appear in the dark areas of the phase images. This means that PMMA does not mix with UHMWPE at the molecular level. This can be understood that in the in-situ polymerization process amorphous PMMA precipitates in both the $scCO_2$ and the $scCO_2$-swollen UHMWPE. This is because the UHMWPE/PMMA polymer pair is thermodynamically immiscible,[27] and PMMA is insoluble in $scCO_2$. The precipitation process[10] is continuous with a constant diffusion, partitioning, and polymerization of MMA monomer within the UHMWPE substrate. Therefore, it is highly likely that the PMMA formed is phase-separated from the UHMWPE amorphous phase.

Figure 9 illustrates the reason why the two amorphous phases cannot be differentiated in Figure 4b by phase imaging. Briefly, at the set point $r_{sp} = 0.79$, the angles of the phase shift for both PMMA and UHMWPE

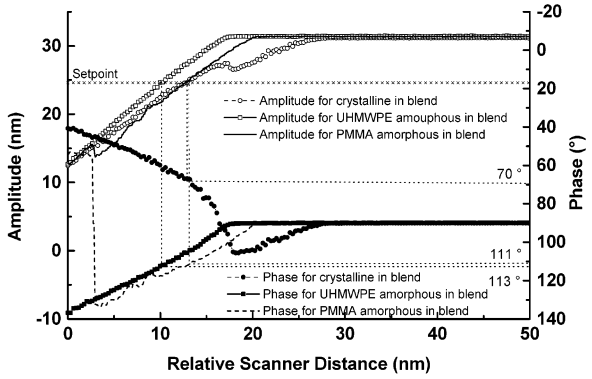

Figure 9. Comparison of the phase shifts between the three domains of the (53/47 w/w) UHMWPE/PMMA blend at the set point amplitude $A_{sp} = 24.5$ nm. The angles of the phase shift for the crystalline, UHMWPE amorphous, and PMMA amorphous phases are 70°, 113°, and 111°, respectively. This explains the reason why these two amorphous phases in the blend could not be distinguished in Figure 4b.

amorphous domains are almost identical at about 111°−113°. It is well-known that APD curves reveal the tip−sample interactions as a function of a tip−sample distance via measurement of amplitude and phase changes against change of tip−sample distance. By contrast the phase image displays the difference between the phase shifts of a sample's different components at one particular tip−sample distance (or amplitude set point). Our current results point out the importance of examining the former when acquiring and analyzing the latter. This is particularly true if a sample investigated involves a multiphase structure like the UHMWPE/PMMA blend examined here, where incorrect conclusions may otherwise be drawn. For example, considering the phase image alone, the PMMA phase is apparently miscible with the amorphous UHMWPE phase. However, the APD measurements clearly indicate that it is indeed phase-separated. This conclusion is supported by the similarity between one of the APD profiles of UHMWPE/PMMA amorphous phase and the "signature" of the pure PMMA. The inability to discriminate the amorphous PMMA and amorphous UHMWPE domains by phase imaging is because the phase lags of amorphous UHMWPE and PMMA are too close to be resolved under a "constant amplitude" feedback control (see Figure 9). This is further demonstrated in Figure 11c where the phase shift angles of these two domains are completely overlapped into one Gaussian distribution.

Although the PMMA and amorphous UHMWPE are phase-separated, the extent of this separation is limited. This is indicated by the phase image in Figure 4b, in which the maximum domain size of the amorphous phases is approximately 100 nm, as estimated from the distance between the crystallites. It is clear that the formation of large-sized PMMA domains is restricted by the rigid UHMWPE crystallites.[10] This value can hence be regarded as the upper limit of PMMA domain dimensions. The minimum PMMA domain size is the contact area between the AFM tip and polymer surface; otherwise, the difference in the APD curves of Figure 7b,c would not have been detected. A reasonable estimate of this contact dimension would be 10 nm. Hence, PMMA domain dimensions are between 10 and 100 nm.

It is shown in Figures 2b and 4b that the incorporation of the PMMA component affects the morphology of the UHMWPE crystallites. The lamellar stacks (bright

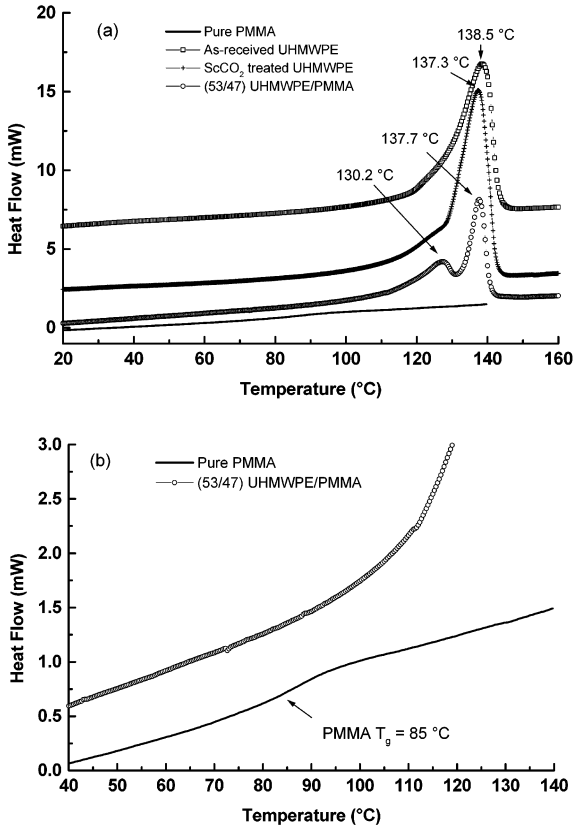

Figure 10. (a) DSC traces for all samples examined at a heating rate of 10 °C min^{-1}, showing an obvious low T_m crystalline melting peak at 130.2 °C for (53/47) UHMWPE/PMMA blend and a hidden no-obvious T_m peak at a similar temperature for $scCO_2$-treated UHMWPE. (b) Enlarged view of DSC traces for the blend and pure PMMA, showing that the T_g of the PMMA component in UHMWPE/PMMA blend is obscured by the endothermic process of the UHMWPE crystalline component.

region) are clearly seen in Figure 2b for the as-received UHMWPE. It is likely that most of these lamellae were viewed edge-on with the lamellar thickness of about 10−40 nm, which is within the range of the reported values.[28,29] This dimension range can be considered as "apparent" since the exact inclination of the crystals to the microtomed sample surface plane is unknown. Whereas the continuity of the UHMWPE lamellae was disrupted to a lesser degree after $scCO_2$ treatment (Figure 3b), Figure 4b shows that this continuity was nearly completely broken up into separate crystallites after addition of PMMA into UHMWPE. This may be caused by the partial melting of the UHMWPE crystallites at the synthesis temperature of 120 °C, which is near the melting temperature of these crystallites as illustrated in Figure 10. The MMA monomers together with $scCO_2$ then diffuse into the molten regions, where the MMA subsequently polymerizes. Therefore, the crystallites are separated by the final PMMA precipitation.

It is also observed in comparison to Figure 2b that the population of small crystallites increases considerably. In the literature,[30,31] these small crystallites are regarded as less perfect crystals and exhibit a low melting temperature because of the short fold length, which means there is a relatively large surface area compared with the volume of the crystals. In addition, it was found that the DSC trace of the blend exhibits a second low T_m endothermic peak at 130.2 °C beside the

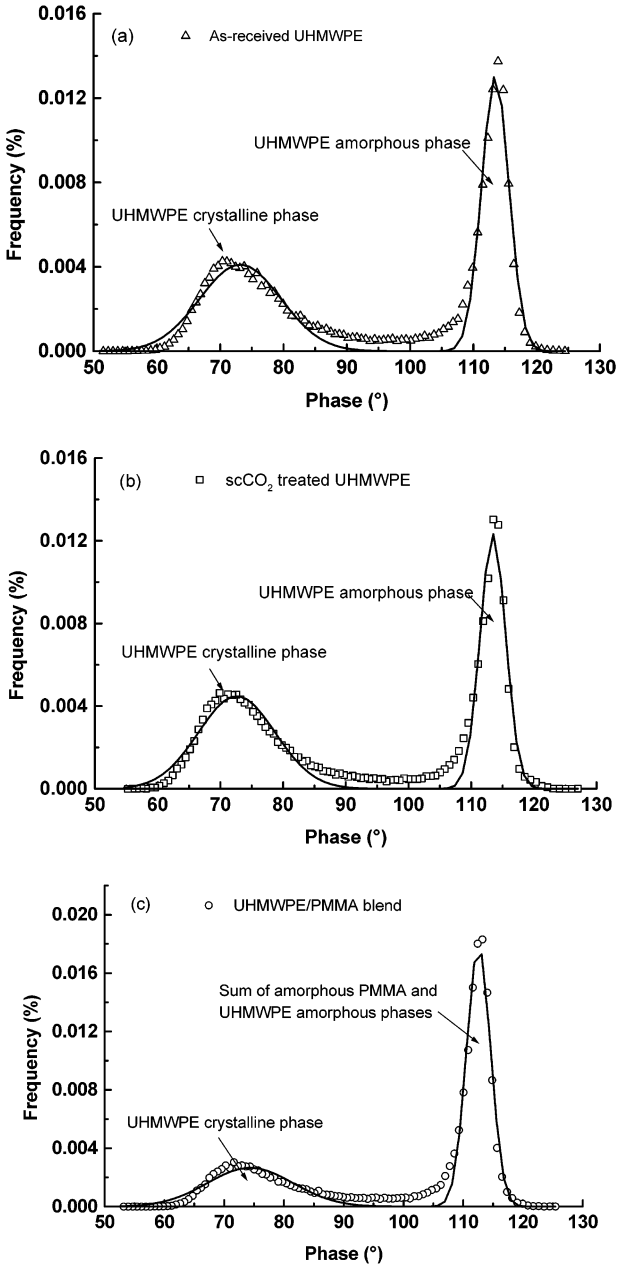

Figure 11. Histograms of the frequency of the pixels as a function of phase shift for sample (a) as-received UHMWPE, (b) $scCO_2$-treated UHMWPE, and (c) (53/47 w/w) UHMWPE/PMMA blend. The data in (a), (b), and (c) are decoded from the phase images of Figures 2, 3, and 4, respectively. The solid lines are Gaussian fitted.

previously observed main crystalline melting peak for UHMWPE at 137.7 °C (Figure 10). This leads us to believe that the increased population of those small crystallites observed in the phase image contributes to the new endothermic peak at 130.2 °C.

The crystallinity was also significantly affected by the in-situ polymerization as shown by the increase from 50.4% for the virgin UHMWPE to 59.2% for the blend (after normalization to the 53 wt % UHMWPE content of the blend, see Table 1).[32] We propose that a large amount of PMMA with relatively small molecular weights, combined with the significant $scCO_2$ swelling effect, enables UHMWPE amorphous chain molecules to become partially disentangled, thereby increasing their mobility at 120 °C. These disentangled molecules are then able to undergo crystallization, because polymers that are normally not in a thermodynamic equilibrium state tend to release their excess free energy by rearranging themselves in a regular manner when sufficient chain mobility is obtained under certain conditions.[33] However, it is not possible for randomly oriented, entangled, and crystallizable polymer chains to crystallize under normal (ambient) conditions because of lack of mobility, and hence they normally remain in the amorphous state.[28]

Table 1. DSC Analysis Results for the Samples Tested at a Heating Rate of 10 °C min^{-1}

samples	ΔH_f (J g^{-1})	T_m (°C)	X_c (%)[a]	normalized X_c (%)[b]
UHMWPE	147.7	138.5	50.4	50.4
$ScCO_2$-treated UHMWPE	154.5	137.3	52.7	52.7
UHMWPE/PMMA blend (53/47 w/w)		137.7		
	91.9		31.4	59.2
		130.2		

[a] Crystallinity in weight percentage based on the heat of fusion for 100% crystalline polyethylene $\Delta H_f = 293$ J g^{-1}.[24] [b] Crystallinity calculated after normalization to the UHMWPE content of the blend in weight.

The change of the crystallinity for the $scCO_2$-treated UHMWPE is not so dramatic, suggesting that the $scCO_2$ swelling alone did not substantially affect the conformations of the UHMWPE molecules. Thus, the PMMA is the main contributor to the enhancement of the UHMWPE chain mobility. However, a slight increase in the crystallinity (Table 1) was indeed observed for $scCO_2$-treated UHMWPE and can also be related to the appearance of a hidden low T_m endothermic peak in its DSC trace (Figure 10a). This relationship is in turn reflected by the slight increase in the number of small crystallites if one compares Figure 2b with Figure 3b. Note that the $scCO_2$-treated UHMWPE and the blend had the same processing thermal history. It is therefore concluded that not only the low T_m but also the increased crystallinity is associated with the additionally small crystallites observed in the phase images (Figures 3b and 4b).

The DSC traces of the pure PMMA and the blend in Figure 10b show that the glass transition temperature (T_g) of the PMMA in the blend was not obvious, as opposed to a clear step change at 85 °C for pure PMMA. This is because a small change in heat capacity at the PMMA T_g was obscured by the large endothermic process of the UHMWPE crystallites below the blend T_m.

Unlike the regular lamellar stacking with uniform chain fold length of 12 nm for solution-crystallized UHMWPE,[34] the thickness of lamellae in the current study is variable. This is not surprising because the chain fold length depends on the thermal history and specific grades of polymer and can be complex for melt-crystallized polymers.[31,32] In theory, the crystalline lamellar thickness, L_c, can be calculated from the melting point of the polymer, T_m, via the Thomson−Gibbs equation:[35]

$$T_m = T_{m0}\left(1 - \frac{2\sigma_e}{L_c \Delta h}\right) \qquad (2)$$

where T_{m0} (418.7 K) is the melting point for a hypothetical crystal of infinite size for which surface energy effects may be ignored.[34] The surface energy of the crystal end faces where the chains fold, σ_e, was taken

to be 9.3×10^{-6} J cm^{-2}. Δh is the heat of fusion of the crystal, which was measured to be 293 J g$^{-1} \approx$ J cm^{-3} (the density of the crystalline is around 0.997−1.005 g cm^{-3}).[24,30] Using the DSC data (Table 1), the lamellar thickness is calculated to be 369 Å at T_m = 138.5 °C. The upper value of the lamellar thickness in Figure 2b is in good agreement with this theoretically calculated value. The thickness of the small, imperfect, and low T_m UHMWPE crystallites observed in Figure 4b is calculated to be 171 Å according to eq 2.

We have also examined the crystalline structure of the UHMWPE at larger scales up to 50 μm (results not shown). It was noted that the polymer does not have a spherulitic morphology that normally occurs in HDPE and other semicrystalline polymers.[10,30,31] This is consistent with recent morphological studies on consolidated UHMWPE resins[36,37] using scanning electron microscopy and transmission electron microscopy. The probable cause for this is that the high molecular weight and high melt viscosity of UHMWPE inhibit the organization of the crystallites.[36]

The potential effect of the blending process on the mechanical properties of the UHMWPE is significant, but in this report, we focus on the morphological study and establishment of TMAFM methodology. In the future, we will continue to report the progress in the testing of the mechanical properties of the composites. Figure 4b demonstrates that there was no large size of amorphous domains (dark regions). Although unfortunately the PMMA phase sizes cannot be directly observed, they can be deduced to be <100 nm as previously described. This fine morphology may help reduce the loss of the impact strength caused by introduction of a brittle polymer.[10]

An estimate of the relative crystallinity of the polymer samples at the microtomed surface can be made from the phase image data presented in Figures 2−4. In these phase images the data value (or intensity) of each pixel is the phase shift recorded at that spatial location. Hence, we propose that a histogram of percentage occurrence of pixel intensity as a function of a phase shift can reveal patterns in the phase data not easily evident in the image alone (see Figure 11). These histograms demonstrate that the angle of the phase shift has a bimodal distribution, which is consistent with the results from the phase images. The lower phase angles in Figure 11 represent the tip responses from the crystalline phase (bright) while the higher phase angles are from the amorphous phase (dark). A distribution of the phase data is to be expected due to topographic effects and instrumental errors. This distribution can be approximately described as Gaussian, as shown by the curve fitted lines in Figure 11. In the curve fitting, two peaks were assigned for UHMWPE and $scCO_2$-treated UHMWPE (Figure 11a,b) in line with their two-phase structures. Although it appears in Figure 11c that the image phase data of the blend can also be described by a bimodal distribution, the data falling within the higher angle peak actually result from both the UHMWPE amorphous and PMMA phases. The data from each of these polymer phases overlap, which is consistent with the APD measurements on the blend as previously demonstrated in Figure 9. The use of the curve fitting allows the crystallinity of the three semicrystalline polymer samples to be quantitatively assessed by calculating the peak areas in the distributions. Accordingly, the crystallinity is 48.3% for UHMWPE, 52.2% for treated $scCO_2$, and 32.8% for UHMWPE/PMMA (i.e., 61.9% of the UHMWPE component). It is found by comparison that the difference between the phase image analysis data and the DSC data (Table 1) is estimated to be less than 5%. Because of practical reasons, we could not give a standard deviation for the phase data. However, we believe that the small error of less than 5% between the two sets of data is close to the precision of these two techniques. The close correlation also reinforces that the acquired phase images in Figures 2−4 represent the nanostructures of UHMWPE, $scCO_2$-treated UHMWPE, and UHMWPE/PMMA blend, respectively.

IV. Conclusions

A one-step, in-situ synthesis of a UHMWPE/PMMA (53/47 w/w) blend was successfully carried out using $scCO_2$ as the processing medium. The morphologies of the resulting blend together with UHMWPE treated and untreated in $scCO_2$ were subsequently characterized with tapping mode atomic force microscopy (TMAFM) and differential scanning calorimetry (DSC). UHMWPE is an ideal model material for TMAFM studies because of the nanoheterogeneity in its morphological structure and its chemical homogeneity. Therefore, the phase image contrast obtained is due unambiguously to a significant difference in stiffness between the crystalline and amorphous phases. The apparent thickness of the crystalline lamellae as estimated from the phase image of the as-received UHMWPE ranges from 10 to 40 nm. This value is in good agreement with a theoretical calculation based on the DSC analysis.

The TMAFM force mode of amplitude−phase−distance (APD) measurement is a very useful method to "fingerprint" multiple components of polymer blends by comparison to "pure" components. The use of the APD measurement demonstrates that the UHMWPE/PMMA blend is a three-phase structure: UHMWPE crystalline and UHMWPE amorphous and PMMA phases with three different characteristic tip−sample interaction profiles. The study also points out the importance to assess the phase images of TMAFM by employing the nonimaging force mode method. On the basis of the size of the AFM probe−sample contact area and the distance between crystallites, the phase-segregated PMMA domains are estimated to be between 10 and 100 nm in size.

The continuity of the UHMWPE lamellae is nearly completely disrupted into separate crystallites by addition of PMMA (Figure 4b). The crystallinity of the UHMWPE/PMMA blend (after normalization) substantially increases to about 59.2%, compared to 50.4% of the pure UHMWPE, as demonstrated by the AFM phase image data and DSC analysis data of the blend. We propose to attribute this increase to the enhanced mobility and partial disentanglement of $scCO_2$-swollen UHMWPE molecules, following incorporation of a large amount of small PMMA molecules into the substrate. Both the increased crystallinity and the second low T_m endothermic peak appeared in the DSC trace of the blend (Figure 10) are associated with the increased population of small thus less perfect crystallites observed in the phase image (Figure 4b).

The crystallinity calculated from phase data analysis for all the semicrystalline polymer samples are in agreement with those determined from DSC. This reinforces that the AFM phase images obtained describe

the nanostructures of UHMWPE and UHMWPE/PMMA blend. Through statistical analysis of the phase distribution in the APD data our results demonstrate that the crystallinity of the samples can be quantified by using phase imaging analysis at 48.3% for UHMWPE, 52.2% for treated $scCO_2$, and 32.8% for UHMWPE/PMMA (i.e., 61.9% of the UHMWPE component). These data are within 5% agreement with standard DSC bulk analysis of crystallinity.

Acknowledgment. We thank the EPSRC Multi-Use Equipment Initiative for funding J.Z. and the EPSRC for a studentship for A.J.B. We thank Dr. M. R. Giles, Miss S. E. Jones, Mr. J. M. Whalley, and Mr. K. Stanley for their advice and technical assistance. We acknowledge also The University of Nottingham Institute of Materials Technology (UNIMAT), and we thank Molecular Profiles Ltd. for access to cryogenic ultramicrotome facilities and Perplas for supplying the UHMWPE used in this study.

References and Notes

(1) Watkins, J. J.; McCarthy, T. J. *Macromolecules* **1994**, *27*, 4845.
(2) Yao, Z. H.; Yin, Z. H.; Sun, G.; Liu, C. Z.; Tong, J.; Ren, L. Q.; Yin, J. H. *J. Appl. Polym. Sci.* **2000**, *75*, 232. Yuan, H.; Hu, P. *J. Appl. Polym. Sci.* **2001**, *81*, 3290.
(3) Mironi-Harpaz, I.; Narkis, M. *J. Polym. Sci., Part B*: *Polym. Phys.* **2001**, *39*, 1415.
(4) Kurtz, S. M.; Muratoglu, O. K.; Evans, M.; Edidin, A. A. *Biomaterials* **1999**, *20*, 1659.
(5) Cooper, A. I. *J. Mater. Chem.* **2000**, *10*, 207. Clarke, M. J.; Howdle, S. M.; Jobling, M.; Poliakoff, M. *J. Am. Chem. Soc.* **1994**, *116*, 8621. Cooper, A. I.; Howdle, S. M.; Hughes, C.; Jobling, M.; Kazarian, S. G.; Poliakoff, M.; Shepherd, L. A.; Johnston, K. P. *Analyst* **1993**, *118*, 1111. Clarke, M. J.; Cooper, A. I.; Howdle, S. M.; Poliakoff, M. *J. Am. Chem. Soc.* **2000**, *122*, 2523. Webb, P. B.; Marr, P. C.; Parsons, A. J.; Gidda, H. S.; Howdle, S. M. *Pure Appl. Chem.* **2000**, *72*, 1347. Howdle, S. M.; Ramsay, J. M.; Cooper, A. I. *J. Polym. Sci., Part B: Polym. Phys.* **1994**, *32*, 541. Kendall, J. L.; Canelas, D. A.; Young, J. L.; DeSimone, J. M. *Chem. Rev.* **1999**, *99*, 543.
(6) McHugh, M. A.; Krukonis, V. J. *Supercritical Fluid Extraction: Principles and Practice*, 2nd ed.; Butterworth-Heinemann: London, 1994.
(7) Hyatt, J. A. *J. Org. Chem.* **1984**, *49*, 5097.
(8) Howdle, S. M.; Watson, M. S.; Whitaker, M. J.; Popov, V. K.; Davies, M. C.; Mandel, F. S.; Wang, J. D.; Shakesheff, K. M. *Chem. Commun.* **2001**, 109.
(9) Watkins, J. J.; McCarthy, T. J. *Macromolecules* **1995**, *28*, 4067. Rajagopalan, P.; McCarthy, T. J. *Macromolecules* **1998**, *31*, 4791.
(10) Kung, E.; Lesser, A. J.; McCarthy, T. J. *Macromolecules* **1998**, *31*, 4160.
(11) Shieh, Y. T.; Su, J. H.; Manivannan, G.; Lee, P. H. C.; Sawan, S. P.; Spall, W. D. *J. Appl. Polym. Sci.* **1996**, *59*, 695. Shieh, Y. T.; Su, J. H.; Manivannan, G.; Lee, P. H. C.; Sawan, S. P.; Spall, W. D. *J. Appl. Polym. Sci.* **1996**, *59*, 707.
(12) Bar, G.; Thomann, Y.; Brandsch, R.; Cantow, H. J.; Whangbo, M. H. *Langmuir* **1997**, *13*, 3807.
(13) Magonov, S. N.; Cleveland, J.; Elings, V.; Denley, D.; Whangbo, M. H. *Surf. Sci.* **1997**, *389*, 201.
(14) Tamayo, J.; Garcia, R. *Langmuir* **1996**, *12*, 4430.
(15) Raghavan, D.; Gu, X.; Nguyen, T.; VanLandingham, M.; Karim, A. *Macromolecules* **2000**, *33*, 2573.
(16) Bar, G.; Ganter, M.; Brandsch, R.; Delineau, L.; Whangbo, M. H. *Langmuir* **2000**, *16*, 5702. Knoll, A.; Magerle, R.; Krausch, G. *Macromolecules* **2001**, *34*, 4159. Chen, X.; McGurk, S. L.; Davies, M. C.; Roberts, C. J.; Shakesheff, K. M.; Tendler, S. J. B.; Williams, P. M.; Davies, J.; Dawkes, A. C.; Domb, A. *Macromolecules* **1998**, *31*, 2278.
(17) Clarke, S.; Davies, M. C.; Roberts, C. J.; Tendler, S. J. B.; Williams, P. M.; Lewis, A. L.; O'Byrne, V. *Macromolecules* **2001**, *34*, 4166.
(18) Danesh, A.; Chen, X.; Davies, M. C.; Roberts, C. J.; Sanders, G. H. W.; Tendler, S. J. B.; Williams, P. M.; Wilkins, M. J. *Langmuir* **2000**, *16*, 866.
(19) Chen, X.; Davies, M. C.; Roberts, C. J.; Tendler, S. J. B.; Williams, P. M.; Davies, J.; Dawkes, A. C.; Edwards, J. C. *Ultramicroscopy* **1998**, *75*, 171.
(20) Chen, X.; Davies, M. C.; Roberts, C. J.; Tendler, S. J. B.; Williams, P. M.; Burnham, N. A. *Surf. Sci.* **2000**, *460*, 292.
(21) Cleveland, J. P.; Anczykowski, B.; Schmid, A. E.; Elings, V. B. *Appl. Phys. Lett.* **1998**, *72*, 2613. Bar, G.; Brandsch, R.; Bruch, M.; Delineau, L.; Whangbo, M. H. *Surf. Sci.* **2000**, *444*, L11.
(22) Kruger, D.; Anczykowski, B.; Fuchs, H. *Ann. Phys. (Leipzig)* **1997**, *6*, 341.
(23) Baker, A. A.; Miles, M. J.; Helbert, W. *Carbohydr. Res.* **2001**, *330*, 249.
(24) Wunderlich, B.; Cormier, C. M. *J. Polym. Sci., Polym. Phys. Ed.* **1967**, *5*, 987.
(25) Sauer, B. B.; McLean, R. S.; Thomas, R. R. *Langmuir* **1998**, *14*, 3045. Bar, G.; Thomann, Y.; Whangbo, M. H. *Langmuir* **1998**, *14*, 1219.
(26) Magonov, S. N.; Elings, V.; Whangbo, M. H. *Surf. Sci.* **1997**, *375*, L385.
(27) Schulze, U.; Pompe, G.; Meyer, E.; Janke, A.; Pionteck, J.; Fiedlerova, A.; Borsig, E. *Polymer* **1995**, *36*, 3393.
(28) Keller, A.; Cheng, S. Z. D. *Polymer* **1998**, *39*, 4461.
(29) Kurtz, S. M.; Pruitt, L.; Jewett, C. W.; Crawford, R. P.; Crane, D. J.; Edidin, A. A. *Biomaterials* **1998**, *19*, 1989.
(30) Bassett, D. C. *Principles of Polymer Morphology*; Cambridge University Press: Cambridge, 1981.
(31) Wunderlich, B. *Macromolecular Physics*; Academic Press: New York, 1973; Vol. 1.
(32) We later produced the other sample blend (59/41 w/w) UHMWPE/PMMA in similar conditions. The DSC thermogram also revealed a significant increase in the crystallinity of the blend (after the normalization to account for the weight ratio of the PMMA component).
(33) Handa, Y. P.; Zhang, Z. Y.; Roovers, L. *J. Polym. Sci., Part B: Polym. Phys.* **2001**, *39*, 1505.
(34) Rastogi, S.; Spoelstra, A. B.; Goossens, J. G. P.; Lemstra, P. J. *Macromolecules* **1997**, *30*, 7880.
(35) Hoffman, J. D.; Davis, G. T. *Treatise on Solid State Chemistry*; Plenum Press: New York, 1976; Vol. 13.
(36) Farrar, D. F.; Brain, A. A. *Biomaterials* **1997**, *18*, 1677.
(37) Olley, R. H.; Hosier, I. L.; Bassett, D. C.; Smith, N. G. *Biomaterials* **1999**, *20*, 2037.

MA012258V